PNAS RESEARCH ARTICLE | CHEMISTRY

Tailoring atomic chemistry to refine reaction pathway for the most enhancement by magnetization in water oxidation

Tianze Wu[a,1], Jingjie Ge[b,1], Qian Wu[a,1], Xiao Ren[c], Fanxu Meng[a], Jiarui Wang[a], Shibo Xi[d], Xin Wang[e], Kamal Elouarzaki[a,f], Adrian Fisher[g,h], and Zhichuan J. Xu[a,f,h,i,2]

Edited by Alexis Bell, University of California, Berkeley, CA; received October 26, 2023; accepted March 22, 2024

Water oxidation on magnetic catalysts has generated significant interest due to the spin-polarization effect. Recent studies have revealed that the disappearance of magnetic domain wall upon magnetization is responsible for the observed oxygen evolution reaction (OER) enhancement. However, an atomic picture of the reaction pathway remains unclear, i.e., which reaction pathway benefits most from spin-polarization, the adsorbent evolution mechanism, the intermolecular mechanism (I2M), the lattice oxygen-mediated one, or more? Here, using three model catalysts with distinguished atomic chemistries of active sites, we are able to reveal the atomic-level mechanism. We found that spin-polarized OER mainly occurs at interconnected active sites, which favors direct coupling of neighboring ligand oxygens (I2M). Furthermore, our study reveals the crucial role of lattice oxygen participation in spin-polarized OER, significantly facilitating the coupling kinetics of neighboring oxygen radicals at active sites.

oxygen evolution reaction | magnetic domain wall | atomic chemistry | magnetic field

Significance

Water oxidation on magnetic catalysts can be promoted by magnetization of the catalysts, raising significant interest in the mechanisms behind it. This study reveals the important fundamentals of the reaction pathway that benefits most from the magnetization of ferromagnetic catalysts for water oxidation. It provides essential guidelines for ferromagnetic catalyst design and highlights the importance of tailoring atomic chemistry to maximize such enhancement.

Given the criticality of climate change, the adoption of advanced technologies has become crucial for achieving a sustainable energy future. The development of reliable and efficient technologies for the harnessing and storage of renewable energy is an essential aspect of this endeavor. In this regard, the production of green hydrogen through renewable electricity-powered water electrolysis is particularly promising owing to its environmental sustainability and potential for widespread availability. Despite its potential as a clean energy source, the practical implementation of green hydrogen production still faces several challenges to make it an efficient and viable option on a worldwide scale (1). One of the major challenges in electrochemical processes is the oxygen evolution reaction (OER) anodic process, which is a slow and energy-intensive four-electron process. This process leads to substantial energy loss, thereby decreasing overall efficiency (2, 3).

The process of OER involves complex multielectron and multistep reactions and intermediates like *OOH, *O, and *OH have a strong linear correlation in adsorption-free energy (4). However, this correlation cannot be independently optimized on a single catalytic site. This complexity highlights the need for a comprehensive approach to achieve optimal results in catalysis. To tackle this challenge, researchers have made significant progress in designing electrocatalysts that address the scaling relationships between binding energies of intermediates and transition states (5). Although there has been progress in catalyst design (6–8), the scaling relation remains a hindrance to further optimization of catalytic activities beyond the volcano plot (9). As a result, an advancement is needed for OER enhancement that can overcome or bypass the limitations of adsorption-energy scaling relations. One potential solution is the use of magnetic fields to overcome scaling relationships for intermediates and transition states with different spin-multiplicity, which inevitably occur in OER. Recent studies suggest that the magnetic properties of reaction intermediates play a crucial role in the kinetics of OER (10). As a result, exposure to an external magnetic field has been shown to significantly improve OER (11–13), which is distinct from the benefits observed in bubble removal via magnetic fields (14, 15). The magnetization's impact on OER goes beyond just enhancing the process itself. It also sheds light on the spin-related fundamentals at play. Researchers predict that when spin flipping occurs during the rate-limiting steps of OER, it creates additional barriers both energetically and kinetically for O_2 turnover in its ground state (triplet) (16). This insight could pave the way for breakthroughs in this area of research. The establishment of quantum spin exchange interactions between intermediates and a ferromagnetic catalytic surface through the introduction of open-shell ferromagnetic spin ordering on catalysts can create spin-sensitive pathways that eliminate the need for spin flipping, resulting in low energy barriers for OER (17, 18). Our latest findings suggest that the rise in magnetization triggers OER by

Author contributions: T.W. and Z.J.X. designed research; T.W., J.G., Q.W., X.R., F.M., J.W., S.X., and Z.J.X. performed research; T.W., J.G., and Z.J.X. contributed new reagents/analytic tools; T.W., J.G., Q.W., S.X., X.W., A.F., and Z.J.X. analyzed data; and T.W., Q.W., K.E., and Z.J.X. wrote the paper.

The authors declare no competing interest.

This article is a PNAS Direct Submission.

[1]T.W., J.G., and Q.W. contributed equally to this work.

[2]To whom correspondence may be addressed. Email: xuzc@ntu.edu.sg.

This article contains supporting information online at https://www.pnas.org/lookup/suppl/doi:10.1073/pnas.2318652121/-/DCSupplemental.

Published April 30, 2024.

eliminating domain walls, leading to a catalyst surface that is entirely covered by a magnetic domain (19). This spin-polarized surface is where OER takes place (19). Despite significant advances in the understanding of the mechanisms underlying spin-polarization-promoted OER on magnetic catalysts, there remains a gap in knowledge at the atomic scale. Specifically, it is crucial to determine the impact of magnetic domains on the promotion of OER through spin-polarization. A more comprehensive understanding of this process at the atomic level is necessary to fully grasp the fundamental concepts that have been uncovered thus far.

We have conducted an in-depth examination of the chemical mechanisms underlying magnetization-enhanced OER, focusing on the atomic level and utilizing model catalysts. Our investigation involved the measurement of OER activity in the presence of a magnetic field, utilizing three distinct multiple-domain Fe_3O_4-supported Ni catalysts. The catalysts we studied had Ni sites in different forms: isolated atoms (IAs), clusters, and a continuous coating layer (shell). Our findings indicate that the Ni-shell/Fe_3O_4 catalyst showed the most significant improvement in OER due to magnetization, while the Ni-IAs/Fe_3O_4 catalyst had almost no effect. The boost in OER is primarily due to the interconnected Ni sites present in the domain wall area of Fe_3O_4. When the magnetic field causes the domain walls to disappear, neighboring ligand oxygens at Ni sites can easily connect through a spin-polarized pathway with low barriers. Although the spin polarization of the Fe_3O_4 substrate has a limited impact on the energetics of the adsorbent evolution mechanism (AEM) on isolated Ni sites, the magnetization-induced OER enhancement is closely related to the oxidation of lattice oxygen, which produces ligand oxygen radicals. We propose that this process enables low-barrier O–O radical coupling, facilitated by lattice oxygen oxidation in spin-polarized OER kinetics.

Results and Discussion

Fe_3O_4 is a highly utilized magnetic material due to its spin polarization and magnetization-induced alignment of magnetic domains (20). Additionally, Fe_3O_4 is known for its stability and inertness under alkaline OER conditions (21, 22). In this study, three configurations of Fe_3O_4 catalysts, namely Ni-IAs/Fe_3O_4, Ni-clusters/Fe_3O_4, and Ni-shell/Fe_3O_4 catalysts, were synthesized through a wet-chemical approach as specified in the Method section. The bulk Fe_3O_4 catalysts were decorated by Ni resulting in the form of IAs, clusters, and shell (Fig. 1 *A–C*, *Left*) to achieve these configurations. The powder X-ray diffraction (XRD) patterns (*SI Appendix*, Fig. S1) reveal that the diffraction peaks are exclusively attributed to a pure-phase cubic spinel (Fd-3m), originating from the Fe_3O_4 substrate. There are no significant diffraction features associated with surface Ni species in any of the samples. This is because the surface Ni content on Fe_3O_4 is negligible and is expected to exhibit poor crystallinity. High-resolution transmission electron microscopy (HRTEM) allows for the identification of Ni-clusters and Ni-shell on Fe_3O_4 substrates, as seen in the *Right* panel of Fig. 1 *A–C*. The isolation of Ni atoms on Fe_3O_4 support is challenging due to the low Z contrast of Ni and Fe. In terms of the Fe_3O_4 substrate, the lattice fringes at approximately 4.86 Å and 2.49 Å correspond to the (111) and (311) crystal planes of cubic Fe_3O_4, respectively. *SI Appendix*, Fig. S2 shows the results of the quantitative energy-dispersive X-ray spectroscopy (EDX) analysis, revealing that the Ni content in all samples is approximately 0.2%, 0.7%, and 3.6% in Ni-IAs, Ni-clusters, and Ni-shell samples, respectively. *SI Appendix*, Table S1 confirms the elemental metal ratios in all samples using inductively coupled plasma optical emission spectroscopy (ICP-OES). The distribution of Ni on the surface region of Fe_3O_4 is illustrated in *SI Appendix*, Fig. S3 *A–C* through the elemental mappings, showing how the content of Ni increases from the IAs to the shell.

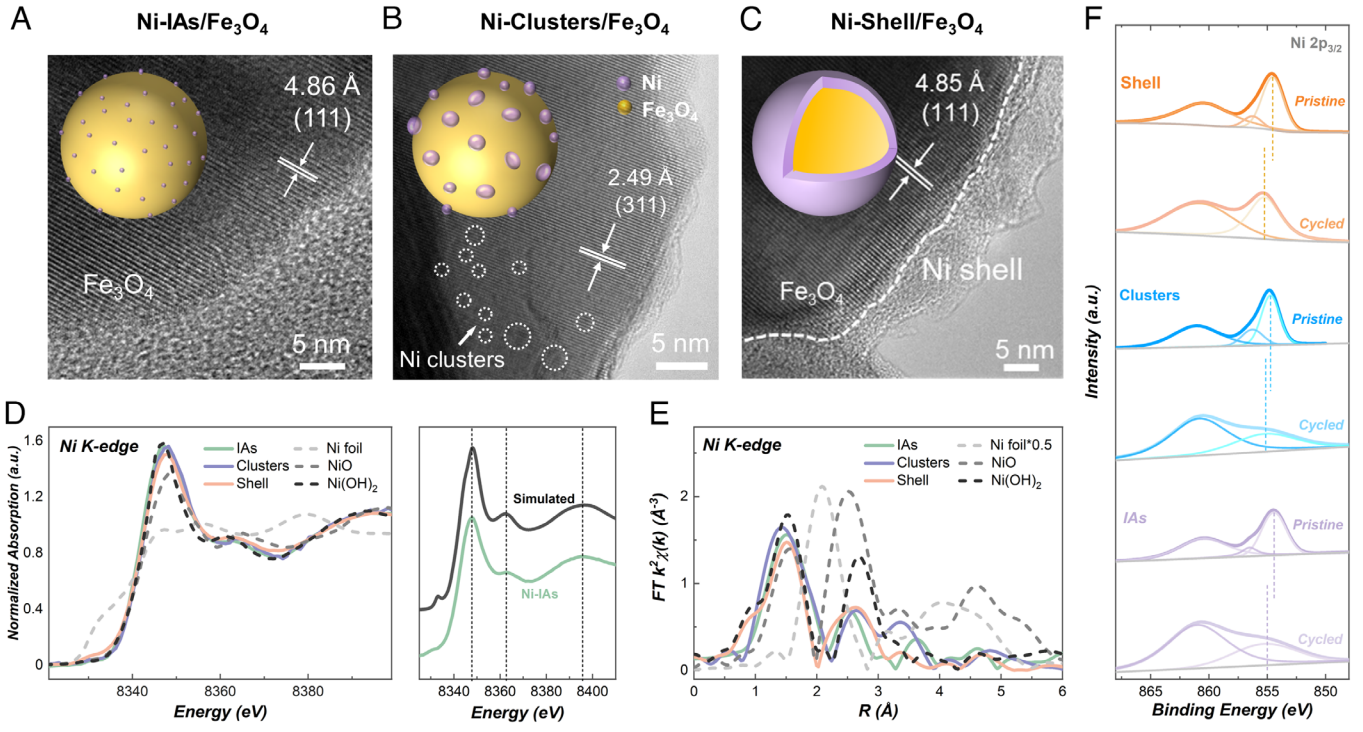

Fig. 1. Structural characterizations of Ni-IAs/Fe_3O_4, Ni-clusters/Fe_3O_4, and Ni-shell/Fe_3O_4. (*A–C*) Schematic illustration of the chemistry (*Inset*) and the corresponding HRTEM image (*Right*) of (*A*) Ni-IAs/Fe_3O_4, (*B*) Ni-clusters/Fe_3O_4, and (*C*) Ni-shell/Fe_3O_4. (*D*) Ni K-edge XANES spectra of Ni-IAs/Fe_3O_4, Ni-clusters/Fe_3O_4, and Ni-shell/Fe_3O_4, in comparison with the spectra of pure Fe_3O_4, referenced Ni foil, NiO, and $Ni(OH)_2$ in *Left* panel. *Right* panel shows a comparison between K-edge XANES of Ni-IAs/Fe_3O_4 (green line) as measured and a simulated one (black line), in which Ni substitutes the Fe at the octahedral site in bulk Fe_3O_4. (*E*) Fourier transform-EXAFS curves of Ni-IAs/Fe_3O_4, Ni-clusters/Fe_3O_4, and Ni-shell/Fe_3O_4, in comparison with the spectra of pure Fe_3O_4, referenced Ni foil, NiO, and $Ni(OH)_2$. (*F*) Ni 2p XPS spectra of Ni-IAs/Fe_3O_4, Ni-clusters/Fe_3O_4, and Ni-shell/Fe_3O_4 before and after CV cycling.

X-ray absorption fine structure (XAFS) analysis was conducted on the prepared catalysts to investigate the atomic structure of Ni species. Fig. 1*D* displays the Ni K-edge X-ray absorption near edge spectra (XANES) of Ni-IAs/Fe_3O_4, Ni-clusters/Fe_3O_4, and Ni-shell/Fe_3O_4, in comparison with the reference spectra of NiO, $Ni(OH)_2$, and Ni foil. The edge position in XANES indicates the oxidation state of Ni (23), with Ni foil at an oxidation state of 0, and NiO or $Ni(OH)_2$ at an oxidation state of +2. Ni's edge features and energies in all as-prepared catalysts are closer to the NiO or $Ni(OH)_2$ than Ni foil, suggesting that the oxidation states of Ni in all prepared catalysts are about +2. In the extended XAFS (EXAFS, Fig. 1*E*), a prominent Ni–O feature (~1.5 Å) is found in Ni-IAs/Fe_3O_4, Ni-clusters/Fe_3O_4, and Ni-shell/Fe_3O_4. The presence of surrounding oxygen atoms coordinated with Ni suggest the major surface chemistry of Ni species to be oxides/hydroxides. The features in the range of 2 to 3 Å observed in Fig. 1*E* are attributed to the metal-metal interactions (24). Specifically, these interactions correspond to the Ni–Ni interactions (~2.64 Å) present in both the Ni-cluster and shell. In the situation of Ni being isolated in Ni-IAs/Fe3O4, it is likely that the interactions between the Ni atoms will be weak. A significant metal–metal interaction (~2.52 Å) was detected, and it cannot be assigned to Ni–Ni interactions. Alternatively, this feature could be ascribed to the Fe–Ni interactions resulting from the substitution of Ni for Fe in Fe_3O_4. A simulation of Ni K-edge XANES was conducted on plausible Ni-substituted Fe_3O_4 models (see *SI Appendix* for simulation details). Ni substitutes Fe at the octahedral or tetrahedral site in both slab and bulk Fe_3O_4 models (*Right* panel of Fig. 1*D* and *SI Appendix*, Fig. S4). Among all simulated models, the one with Ni substitution at octahedral Fe sites of bulk Fe_3O_4 shows the most consistency with the experimental result.

Cyclic voltammetry (CV) of Ni-IAs/Fe_3O_4, Ni-clusters/Fe_3O_4, and Ni-shell/Fe_3O_4 was conducted under O_2-saturated condition in 1.0 M KOH. Alongside our electrochemical experiments, we conducted X-ray photoelectron spectroscopy (XPS) tests to delve deeper into the stability of Ni-IAs/Fe_3O_4, Ni-clusters/Fe_3O_4, and Ni-shell/Fe_3O_4. The goal was to gain a more comprehensive understanding of the alterations in surface chemistry for all catalysts during electrochemical tests. Fig. 1*F* shows that the binding energies of Ni-IAs/Fe_3O_4, Ni-clusters/Fe_3O_4, and Ni-shell/Fe_3O_4 are consistent, at approximately 854.5 eV, which correspond to Ni 2p3/2 of Ni^{2+}. This aligns with the experimental result of $Ni(OH)_2$ (25). After CV cycling, the binding energy peaks shifted to around 855.2 eV, which corresponds to Ni 2p3/2 of Ni^{3+}. This is consistent with the reported deprotonation of $Ni(OH)_2$ to produce NiO_xH_y species during the OER (26, 27). Additionally, the XPS investigation demonstrated the stable chemistry of Fe in Fe_3O_4 substrate form. The binding energies of Ni-IAs/Fe_3O_4, Ni-clusters/Fe_3O_4, and Ni-shell/Fe_3O_4 show little shift after CV cycling (*SI Appendix*, Fig. S5). In *SI Appendix*, Fig. S6, Fe K-edge XANES and EXAFS of Ni-IAs/Fe_3O_4, Ni-clusters/Fe_3O_4, and Ni-shell/Fe_3O_4 further confirm that the profiles of the samples before and after CV cycling are nearly overlapped. The XRD patterns, HRTEM images, and EDX mapping of the cycled samples confirm minimal electrochemical reconstruction and the Fe_3O_4 remains well-maintained (*SI Appendix*, Figs. S7 and S8). Therefore, it is believed that NiO_xH_y is the predominant chemistry of the Ni species on Fe_3O_4 in electrochemical conditions.

CVs were obtained for Ni-IAs/Fe_3O_4, Ni-clusters/Fe_3O_4, and Ni-shell/Fe_3O_4 catalysts in both the presence and absence of a magnetic field. Prior to the magneto-electrochemical experiments, all catalysts were subjected to 50 cycles of CV to achieve a steady state (*SI Appendix*, Fig. S9). The steady-state OER CVs of Ni-IAs/Fe_3O_4, Ni-clusters/Fe_3O_4, Ni-shell/Fe_3O_4, and pure Fe_3O_4 are presented in Fig. 2*A* (dashed line). The magnetic field (0.3 T) was then applied to the electrolysis cell according to our previous set-up (12, 28) and the CV was recorded with the field (Fig. 2*A*, solid line). It has been observed that activity enhancement occurs under a magnetic field, however, the degree of enhancement varies depending on the type of Ni catalysts used. Ni-shell catalysts exhibit the highest level of enhancement, while Ni-clusters and isolated Ni sites show much lower levels of enhancement. The OER current densities with and without magnetic field are shown in Tafel plots (*SI Appendix*, Fig. S10), where the error bars represent at least three independent measurements. Magnetism measurements were carried out to assess the magnetic properties of the catalysts. The M–H (magnetic hysteresis) curves under 3 K for Fe_3O_4, Ni-IAs/Fe_3O_4, Ni-clusters/Fe_3O_4, and Ni-shell/Fe_3O_4 are shown in Fig. 2*B*. The saturated magnetization of Ni-shell/Fe_3O_4 is lower than that of other samples because of the higher content of the paramagnetic NiO_xH_y component. All samples display significant coercivity in M–H measurements due to Fe_3O_4's ferrimagnetic property as a support. The coercivity of Fe_3O_4 at ~177 Oe falls in the reported range for multidomain Fe_3O_4 (29). Additionally, the critical size for the evolution of Fe_3O_4 from single-domain to multidomain is ~76 nm, and the as-synthesized Fe_3O_4 particles are at a size of over 100 nm (29). This confirms that the Fe_3O_4 in this study exists in a multidomain state. Moreover, Fe_3O_4 exhibit a symmetrical hysteresis loop with respect to the *y*-axis. However, when Ni catalysts are applied to the surface of the material, the hysteresis loops display a slightly negative shift, which is commonly referred to exchange bias (30, 31). This phenomenon arises due to the presence of interfacial spins that become pinned and are unable to fully align with the sweeping magnetic field during M–H measurement (13). The exchange bias is notable when Ni sites become more interconnected (shell), whereas it is minimal when the Ni sites are isolated (IAs), as illustrated in Fig. 2*C*. The values of exchange bias for these catalysts show a consistent trend with their activity enhancement by magnetization as summarized at the potential of 1.64 V (Fig. 2*D*). The interfacial exchange bias indicates essential spin channel in the catalysts, which plays an important role in the spin polarization for magnetization-enhanced OER. The Ni-shell/Fe_3O_4 system exhibits a higher exchange bias due to a larger population of spins that are aligned and pinned at the interface. Specifically, the interface spins in the Ni species align with the magnetic domains of the Fe_3O_4 substrate under spin pinning. The utilization of a magnetic field promotes spin polarization in Ni species by aligning magnetic domains in Fe_3O_4, leading to improved OER performance.

In comparing IAs/Fe_3O_4, Ni-clusters/Fe_3O_4, and Ni-shell/Fe_3O_4, the primary distinguishing factor is the distribution of Ni species on Fe_3O_4. The Ni-shell configuration exhibits the lowest average atomic distance between Ni, while Ni-IAs has the largest distance between Ni. This information is depicted in Fig. 1*A*. In regard to Ni species, it is important to note that the rate of OER may be restricted by the O–O coupling process, which is commonly associated with considerable energetic and kinetic barriers (32). The process of O–O coupling can take place through either a single-site or dual-site mechanism (33). Fig. 3*A* illustrates that the AEM for OER involves the attack of H_2O/OH- on a single M–O unit resulting in the formation of M–OOH species. Another pathway for AEM involves the strong interaction between ligand oxygen from two M–O units, completing the coupling [intermolecular mechanism (I2M)].

Several DFT (density functional theory) studies have revealed that I2M may be more energetically favorable than AEM (34–36). To investigate this possibility, we examined the energetics of Ni catalysts with Fe_3O_4 support, calculating the I2M pathways on

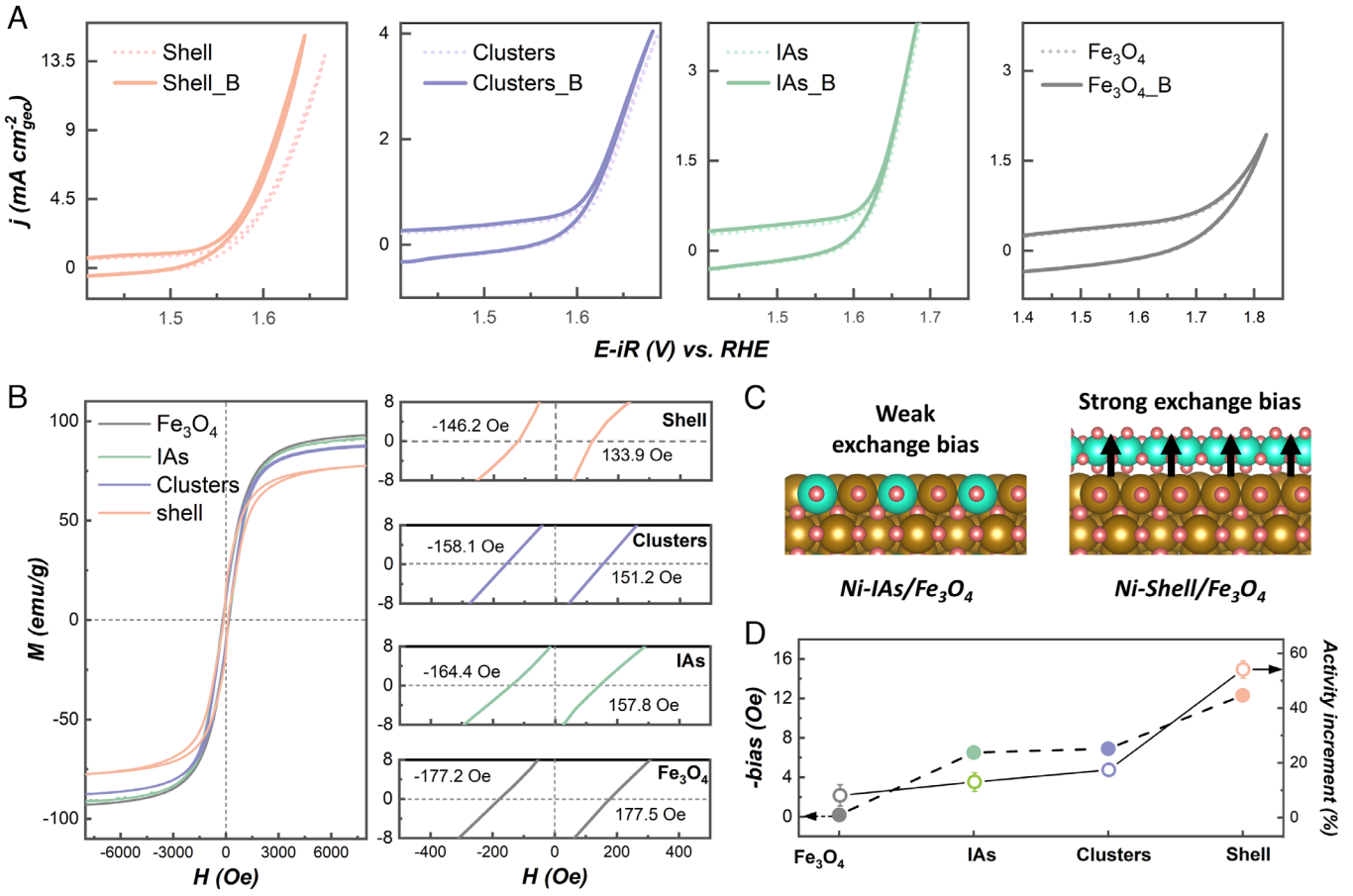

Fig. 2. OER enhancement under a magnetic field. (*A*) OER activities of Ni-IAs/Fe_3O_4, Ni-clusters/Fe_3O_4, and Ni-shell/Fe_3O_4 with (dot line) and without (solid line) an external magnetic field. (*B*) The M–H loops of Fe_3O_4, Ni-IAs/Fe_3O_4, Ni-clusters/Fe_3O_4, and Ni-shell/Fe_3O_4 samples under 3 K (*Left*), and the enlarged M–H loops that intersect with y = 0 axis (*Right*) showing the exchange bias in hysteresis loops. (*C*) The schematics of the exchange bias originating from the spin pinning effect in Ni/Fe_3O_4 configuration. The brown and green atoms denote iron and nickel, respectively. (*D*) The correlation between the exchange bias and the percentage of *j* increment at 1.64 V vs. RHE under the external magnetic field for Fe_3O_4, IAs/Fe_3O_4, Ni-clusters/Fe_3O_4, and Ni-shell/Fe_3O_4.

Ni sites with different Ni–Ni interatomic distance (Fig. 3 *B* and *C*). The O–O coupling with *OH+*O and *O+*O intermediates have been studied. The energetics for O–O coupling with *OH+*O are shown in the Fig. 3 *E* and *F*. The results showed that when the interatomic distance is shorter, the energetic barrier of the O–O coupling process is much lower, at only 0.617 eV. Conversely, with a longer interatomic distance, the energetic barrier for O–O coupling is extremely high, at 2.611 eV. It shows consistent trend when calculating with *O+*O intermediates (*SI Appendix*, Fig. S11 *A* and *B*), but the overall energetics is unfavorable compared to that with *OH+*O intermediates. On a single Ni site (Fig. 3*E*), the OER can follow an AEM pathway, in which the highest energetic barrier is assigned to the electron transfer step from *OOH to * intermediate, at 1.18 eV (Fig. 3*G*). Thus, based on an analysis of reaction energetics, the OER will prefer I2M pathway when two nearby Ni sites are available. However, when the interatomic distance of Ni sites is too long, the OER will prefer the AEM pathway at isolated Ni sites instead. In summary, the OER pathway can be distinguished according to the Ni atomic chemistry in either isolated or interconnected configuration, with I2M highly unlikely on isolated surface Ni sites, and the AEM pathway expected to be dominant. Conversely, in Ni-shell with interconnected Ni atoms, the O–O coupling in low-barrier I2M pathway is favorable.

The diverse improvement of OER performance, when subjected to a magnetic field, can be explained by the distinct magnetization effects that occur through both the AEM and I2M. Ni-IAs, Ni-clusters, and Ni-shell supported on Fe_3O_4 materials are excellent models for demonstrating atomic-scale phenomena. Magnetic materials, such as Fe_3O_4, are made up of multiple ferromagnetic domains which possess polarized spins (37). These domains exhibit disordered magnetizations prior to the application of a magnetic field. The transitional regions between neighboring magnetic domains with different magnetizations, known as domain wall regions, contain electrons with disordered spin directions (38). In Fe_3O_4-supported Ni catalysts, the spins of surface Ni species become aligned by the magnetic domains in the Fe_3O_4 due to the spin pinning effect. When Ni sites weakly bond with adsorbed oxygen ligands, the resulting Ni–O species can be described as having an oxyl configuration. In this configuration, the unpaired d electrons of Ni and unpaired p electrons of the ligand oxygens are in a parallel spin alignment (33). In the context of magnetic domains, the Ni-shell's neighboring ligand oxygens exhibit parallel spin direction. However, a disordered spin pattern is observed for ligand oxygens located in the domain wall region, as shown in Fig. 4*A*. Toward triplet oxygen (↑O=O↑) turnover, additional barriers arise to align the spins of two ligand oxygens, allowing two electrons in parallel spin direction to occupy the π^* antibonding orbitals of O_2. Applying a magnetic field to the catalyst results in highly aligned magnetic domains in Fe_3O_4, which achieves long-range ferromagnetic spin ordering and spin polarization. This leads to the evolution of Fe_3O_4 from a multidomain state to a single-domain state, eliminating the domain wall region. Simultaneously, neighboring ligand oxygens on Ni-shell align to the same spin direction within the domain wall

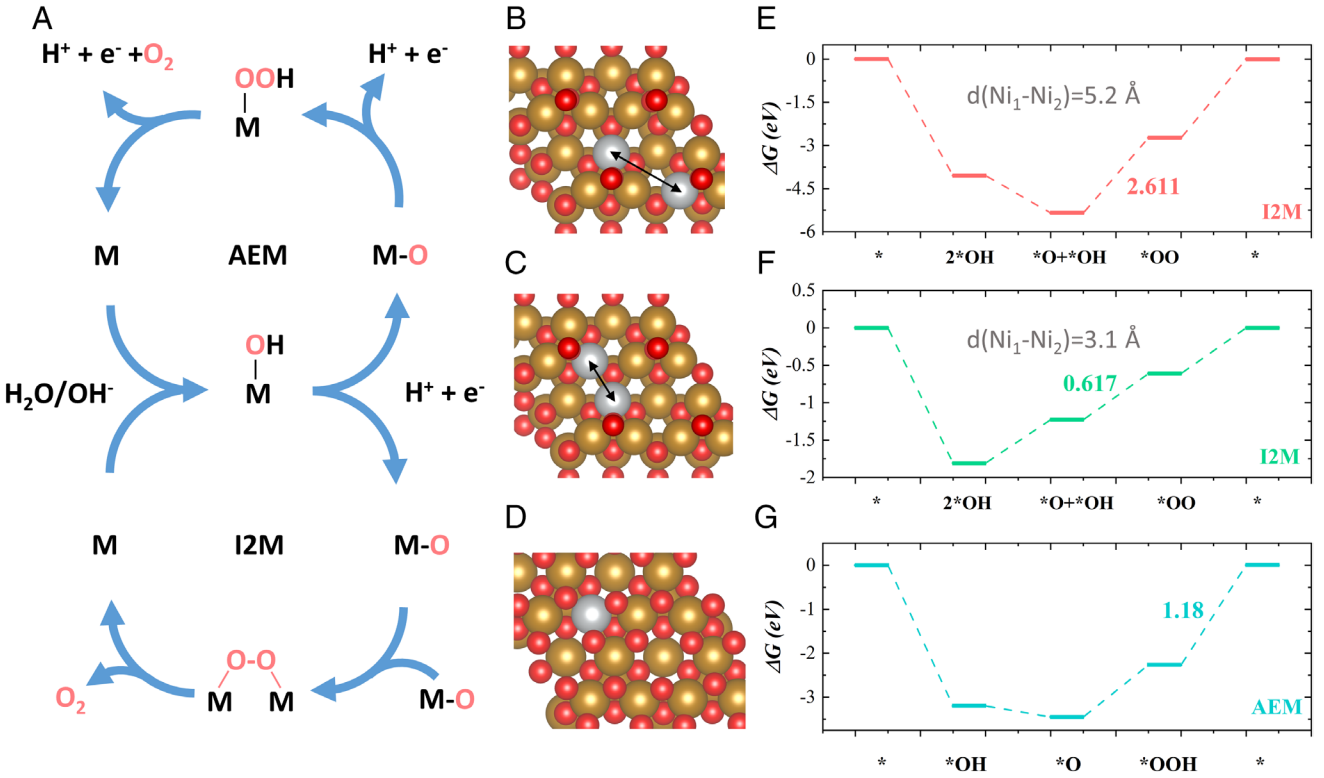

Fig. 3. DFT studies of the energetics on model catalysts. (*A*) The schematics of AEM and I2M OER mechanisms. (*B* and *C*) The computational model for I2M pathway on two Ni sites with (*B*) long and (*C*) short interatomic distance. The support is Fe_3O_4 (111) slab. (*D*) The computational model for AEM pathway on single Ni site. Brown, gray, and red spheres denote iron, nickel, and oxygen, respectively. (*E*–*G*) The Gibbs free energy diagrams along with I2M and AEM reaction coordinates on calculated (*B*–*D*) models.

region, reducing the barrier for subsequent O–O coupling for triplet O_2 turnover. As a result, the OER efficiency is enhanced. This is depicted in Fig. 4 *A*, *Bottom* and Fig. 4*B*.

Based on DFT studies, it has been observed that isolated Ni sites on Fe_3O_4 are more likely to favor AEM mechanism for OER. However, the I2M pathway for OER is expected to be very

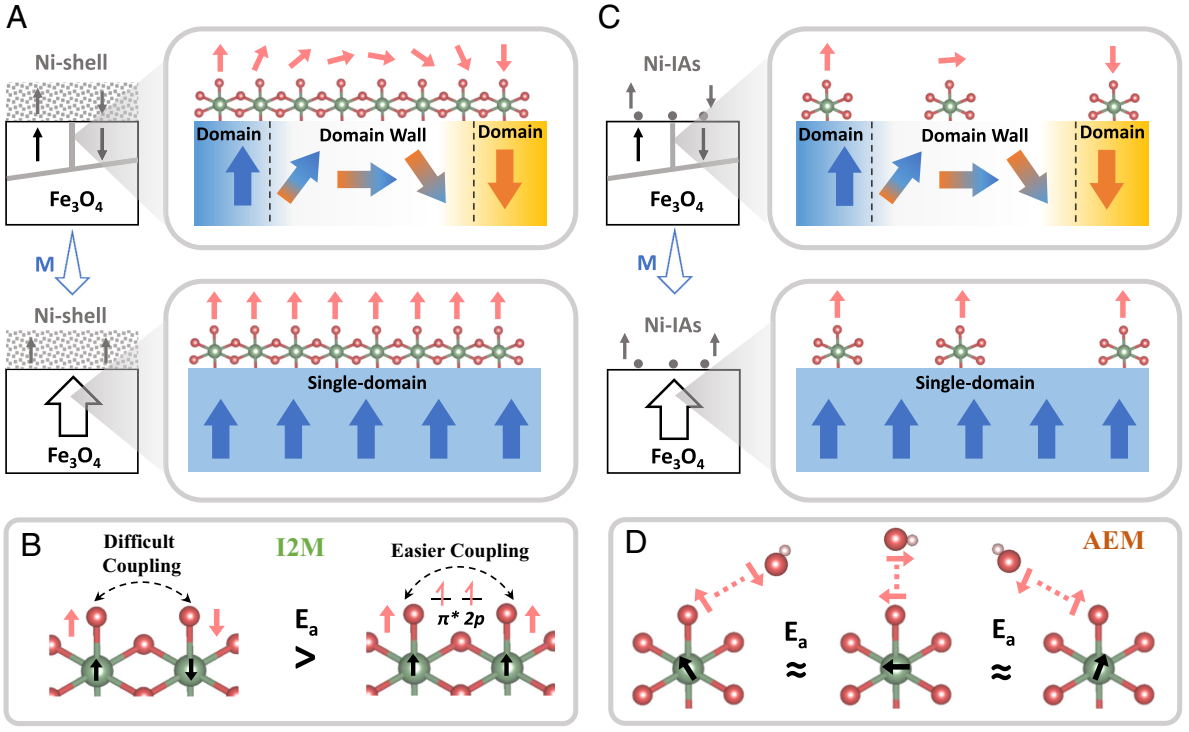

Fig. 4. Atomic-scale magnetization relating to OER mechanisms. (*A*) The schematics of Ni-shell on the magnetic domains of Fe_3O_4 before and after magnetization. (*B*) The illustration of O–O coupling process under I2M mechanism. E_a denotes the activation energy for the coupling of oxygen radicals. (*C*) The schematics of Ni-IAs on the magnetic domains of Fe_3O_4 before and after magnetization. (*D*) The illustration of O–O coupling process under AEM mechanism.

negligible on isolated Ni due to the large atomic distance between them. It is worth noting that the disappearance of the domain wall region under a magnetic field (as seen in Fig. 4*C*) may have an impact on certain isolated Ni sites within this region. Spin-selected electron transfer is likely to be facilitated if the intrinsic spin structure of Ni–O intermediate is optimized and promoting the spin polarization, which benefits the O–O coupling process (Ni–O···OH^-) (33). Enhancing the intrinsic spin structure of Ni by flipping the spins in its d orbitals is unlikely to be triggered by the disappearance of the domain wall. This is because the scale of a single Ni atom is much smaller than that of Ni-clusters and shells, limiting its interaction with the magnetic moments in Fe_3O_4. This is consistent with the weak exchange bias observed in IAs/Fe_3O_4. When a single Ni site maintains its intrinsic spin structure, the O–O coupling in different directions shows almost no difference in energetics (Fig. 4*D*). Although DFT studies have indicated that the spin-sensitive O–O coupling step may not be the potential-limiting step (PLS) under AEM mechanism (Fig. 3*G*), dissociating *OOH toward O_2 turnover poses a greater challenge. While spin polarization can affect the O–O coupling in AEM, its impact on the overall reaction rates is negligible. Therefore, applying a magnetic field is unlikely to significantly affect the OER activity of Ni-IAs/Fe_3O_4.

DFT studies are conducted on the possible I2M O–O coupling pathways on NiOOH. In NiOOH (Fig. 5*A*), the distance between two terminal oxygens resulting from adsorption of OH^- is approximately 2.9 Å. However, the atomic distance between a terminal ligand oxygen and a nearby lattice oxygen is about 2.7 Å. The coupling of two neighboring ligand oxygens exhibits a significantly higher energetic barrier compared to the coupling with one ligand oxygen and one activated ligand oxygen. The models for DFT studies are shown in *SI Appendix*, Fig. S12 *A–C*. The distance between the ligand oxygens linked to the Ni sites plays a crucial role in the O–O coupling energetics. It is advantageous to have two ligand oxygen radicals in close proximity to facilitate direct radical coupling, specifically for O_2 turnover, I2M. Therefore, we propose that involving the lattice oxygen in the radical oxygen coupling process will facilitate the I2M pathway. To carry out radical O–O coupling, the lattice oxygen must be oxidized to create a ligand oxygen radical. Fig. 5*B* illustrates how lattice oxygen can be oxidized to create oxygen holes, which enables ligand oxygen with great radical character. If the electron removal in lattice oxygen oxidation is spin-selective, as enabled by the spin channels in NiOOH, it generates polarized ligand oxygen radicals.

In order to confirm the involvement of the lattice oxygen of surface Ni species in OER, we utilized an ^{18}O-isotope labeled Ni-shell/Fe_3O_4 to monitor the O_2 chemistry during OER using mass spectrometry (MS). The results were measured by detecting the $^{34}O_2$ ($^{16}O^{18}O$) and $^{32}O_2$ ($^{16}O_2$) signals after the OER process, as outlined in *SI Appendix* and Fig. 5*C* for further details. In Fig. 5*D*, we can see the ratio of $^{34}O_2$ to $^{32}O_2$ in the gas product

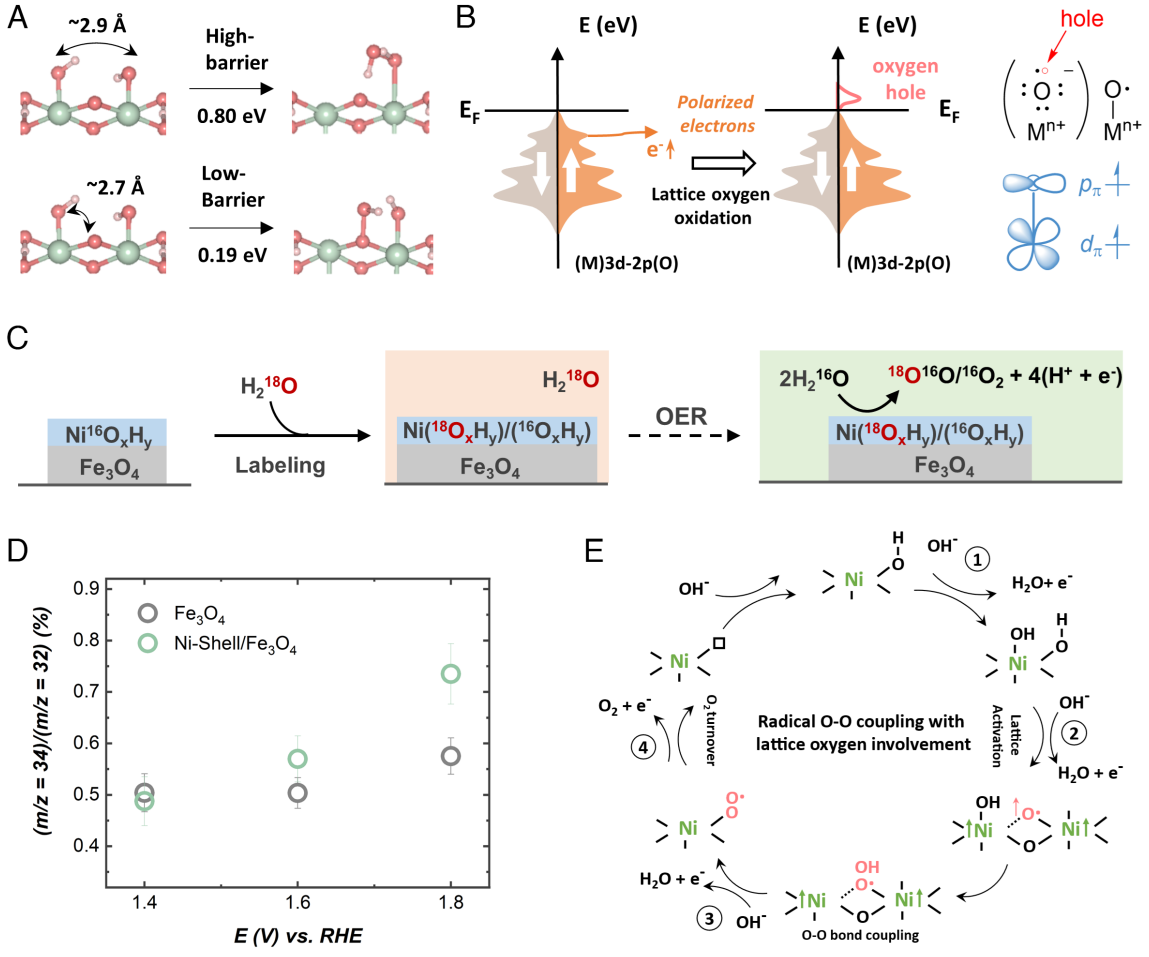

Fig. 5. The critical role of lattice oxygens. (*A*) Energetic barrier of O–O coupling through coupling of two neighboring ligand oxygens or coupling of one terminal ligand oxygen and one activated lattice oxygen. (*B*) The lattice oxygen oxidation and the hole creation to create ligand oxygen radical under spin-polarized electron transfer (33). (*C*) Schematics of the procedure of the isotopic labeling of Ni catalysts on Fe_3O_4 with $K^{18}OH$ electrolyte. The stable surface NiO_xH_y on Fe_3O_4 was derived by electrochemical conditioning of Ni-shell/Fe_3O_4 with 50 CVs in 1 M $K^{16}OH$ at a scan rate of 20 mV s^{-1} between 1.1 to 1.85 V vs. RHE. (*D*) Oxygen isotope ratio of $^{18}O^{16}O$ to $^{16}O_2$ produced by the tested samples as a function of applied potentials in CV measurements. (*E*) The OER mechanism on Ni species, in which the O–O coupling process involving the activation of lattice oxygens.

after conducting chronoamperometric (CA) tests at different potentials (1.4, 1.6, and 1.8 V vs. RHE) for Ni-shell/Fe_3O_4 and bare Fe_3O_4. The results show that the Ni-shell/Fe_3O_4 exhibits a higher ratio of $^{34}O_2$ to $^{32}O_2$ at potentials above 1.6 V, indicating that the primary $^{34}O_2$ signal comes from the Ni-shell rather than the Fe_3O_4 substrate. It is also observed that the potential region (>1.6 V vs. RHE) where lattice oxygen is involved in OER corresponds to the potential region where OER enhancement under a magnetic field was observed. It is also noted that pure Fe_3O_4 shows little enhancement by magnetization, which can be attributed to the stable lattice chemistry within the investigated potential window (39). The lattice oxygen oxidation should be an important trigger of OER enhancement under a magnetic field by promoting the O–O radical coupling. The involvement of lattice oxygen in the radical O–O coupling for O_2 turnover is illustrated in Fig. 5*E*. The first ligand oxygen radical is generated by the deprotonation of a lattice oxygen in NiOOH. Another ligand oxygen radical is created by the lattice oxygen oxidation. The atomic distance of these two oxygen radicals is the closest among all available atomic O–O distance in the NiOOH model. Besides, the ligand oxygens associated with a single metal site or two spin-polarized metal sites should exhibit parallel spin alignment. The energetic and kinetic barriers can be very low in the coupling of the two nearby ligand oxygen radicals without spin flipping, which evolves the O_2 in its ground state (triplet). Understanding the favorable pathway for OER enhancement through magnetization opens up significant opportunities for electrocatalyst design to maximize spin-related enhancements in OER. Activating lattice oxygen to create more ligand oxygen radicals, for instance, by uplifting O 2p level close to Fermi level in oxides (40, 41). shows promise for further enhancing OER under magnetic fields.

Conclusion

In summary, we have demonstrated the OER mechanism for observed magnetization-caused enhancement using Ni-IAs/Fe_3O_4, Ni-clusters/Fe_3O_4, and Ni-shell/Fe_3O_4, as model catalysts. The OER improvement by magnetization varies among these model catalysts. The interconnected Ni–O units can carry out I2M on two ligand oxygens, while AEM will be dominant as Ni sites become isolated. The I2M happening at the domain wall region is believed to be promoted in a spin-polarized manner by magnetization as the spin polarization occurs. In addition, the I2M on the Ni-shell can be energetically more favorable as the OER kinetics involve the lattice oxygen participation creating more nearby ligand oxygen radicals. For isolated Ni sites with AEM pathway, their spin structure at a single atom scale is less affected by the spin polarization in Fe_3O_4. The spin-sensitive O–O coupling process is not the PLS in AEM pathway. Therefore, the OER can hardly be improved on Ni-IAs under a magnetic field but showing notable increment on Ni-shell. Overall, the OER enhancement by magnetization depends on not only the spin polarization of catalysts but also the atomic configuration of active sites over the magnetic domains. Our methodologies have uncovered significant insights into the atomic-scale mechanisms underlying magnetization-enhanced OER on magnetic catalysts, thus contributing toward a comprehensive understanding of this process.

Materials and Methods

Chemicals. Iron(II, III) oxide (<5 μm), nickel (II) nitrate hexahydrate (99.999% trace metals basis), nickel (II) acetylacetonate (95%), sodium borohydride (ReagentPlus®, 99%), hexadecylamine (technical grade, 90%), mesitylene (98%), and potassium hydroxide (semiconductor grade, pellets, 99.99% trace metals basis) were all from Sigma-Aldrich. Methanol (MeOH), ethanol (EtOH), and isopropanol were purchased from Merck. Milli-Q deionized water (DI water, 18.2 MΩ·cm) was used in all experiments.

Synthesis of Ni-IAs/Fe_3O_4, Ni-Clusters/Fe_3O_4. The Ni-IAs/Fe_3O_4 and Ni-clusters/Fe_3O_4 were synthesized according to the following method (42). The Ni-IAs catalyst was prepared as follows: 1 mg of $Ni(NO_3)_2{\cdot}6H_2O$ was dissolved in 20 mL MeOH by ultrasound for 20 min in r.t. The mixture solution was slowly added to 5 mL of meOH solution of dispersed bulk Fe_3O_4 (1 mg mL^{-1}) and further stirred at r.t. for 1 h. Then, 5 mg of $NaBH_4$ dissolved in ice water was dropwise added to the above solution and further stirred for 10 min. The suspension of Fe_3O_4 loaded with Ni atoms was filtered. The precipitate was washed with DI water and EtOH for 5 times to remove the soluble ions and kept for further use. Ni-clusters/Fe_3O_4 was prepared according to the same protocol, except the 4 mg $Ni(NO_3)_2{\cdot}6H_2O$ was added.

Synthesis of Ni-Shell/Fe_3O_4 Catalysts. The Ni-shell/Fe_3O_4 was prepared by a wet-chemical method (21) as follows: $Ni(acac)_2$ (8 mg) and HDA(80 mg) were added into mesitylene(10 mL) to obtain a homogeneous solution, followed by the addition of Fe_3O_4 (16 mg). The Fe_3O_4 particles were dispersed by 20-min ultrasonication. A dispersion was transferred to a Synthware press bottle. The reaction was conducted in two stages in the oil bath under stirring: At the first stage, the temperature was increased to 170 °C and kept for 60 min; at the second stage, the temperature was further increased to 200 °C and held for 75 min. The reactor was then cooled down to r.t. The as-prepared Ni-shell/Fe_3O_4 was obtained after being centrifugated and washed by EtOH.

Structural Characterization. TEM and EDS were all conducted by JEOL JEM-2100F. An acceleration voltage was kept at 200 keV. Before TEM observation, all samples in powder form were well dispersed in EtOH. The uniform ink was then dropped onto holey carbon-supported copper grids, which was then dried for 12 h at room temperature. XRD was performed with Cu-K_α radiation ($\lambda = 1.5418$ Å) on Shimadazu XRD-6000. XPS was carried out on a Shimadzu Kratos Axis Supra instrument and a monochromatic Al-K_α X-ray source was used for XPS measurement. The energy of XPS data was calibrated according to the C 1s spectra. Using the Lorentz Gaussian fitting method, the XPS spectra of Ni 2p have been deconvoluted into smaller contributions as shown in Fig. 1*F* and *SI Appendix*, Fig. S5. ICP-OES measurements were performed on Agilent 720 Series ICP-OES. The magnetism of materials was studied by the Superconducting Quantum Design magnetometer (MPMS-XL). The M–H curves for measuring exchange bias were recorded at a temperature of 2 K under magnetic fields switching between −5 and +5 T. The XAFS was performed at beamline XAFCA of the Singapore Synchrotron Light Source to obtain structural information (43). The spectra were recorded in the transmission mode for Fe K-edge and fluorescence emission mode for Ni K-edge. The X-ray fluorescence characterization was conducted by using a silicon drift detector. Utilizing the ATHENA module of the IFEFFIT software packages, the obtained EXAFS data were performed according to the standard procedures (44). The k^2 -weighted EXAFS spectra were drawn through postedge background subtraction from the overall absorption and normalizing in terms of the edge jump step. Subsequently, the EXAFS contributions were separated from different coordination shells by using a Hanning window ($dk = 1.0$ $Å^{-1}$), then k^2-weighted $\chi(k)$ data of Fe K-edge and Ni K-edge were Fourier transformed to real (R) space.

DFT Calculations. The DFT studies were carried out by the Vienna Ab initio Simulation Package (45). The ion-electron interaction described by the projected augmented wave model has been involved in our study (45). We consider the correlation-exchange effects according to Perdew–Burke–Ernzerhof functional (46) of the generalized gradient approximation. We performed GGA + U calculations in our studies and the calulation was carried out on the model proposed by Dudarev et al. (47). U_{eff} (U_{eff} = Coulomb U – exchange J) values for iron cations, nickel cations in tetrahedral sites, and nickel cations in octahedral sites have been given as 4.0 eV, 6.0 eV, and 6.4 eV, respectively. The cutoff energy was set to be 450 eV for all the calculations. The (110) surface was cleaved with five atomic layers. The Monkhorst−Pack (48) k-point mesh was set to be 6 × 6 × 6 and 3 × 2 × 1 for optimizing the structure of Ni-substituted Fe sites of Fe_3O_4 with bulk and surface models, respectively. The NiOOH (100) surface was cleaved with four atomic layers to investigate the O–O coupling process. The Monkhorst−Pack k-point mesh was set to be 2 × 5 × 1 for optimizing the structure NiOOH (100) slab.

Electrochemical Tests and Analysis. The OER was measured using a three-electrode electrolysis cell. The working electrode was fabricated by drop-casting catalysts on carbon papers (2 × 2 cm^2). Pt plate (1 × 2 cm^2) was used as the counter electrode, and Hg/HgO (aqueous, 1 M KOH) served as the reference electrode. To prepare the ink of catalysts, a catalyst of 4 mg was dispersed in a solvent, which consists of 25 μL Nafion perfluorinated resin solution (5 wt% in water), 200 μL Isopropyl alcohol, and 775 μL water. The dispersion was ultrasonicated for at least 30 min to become homogeneous. The working electrode was prepared by drop-casting on carbon paper (effective surface area is 4 cm^2). The mass loading on the electrode is 90 $\mu g_{catalyst}\ cm^{-2}$. Biologic SP 150 potentiostat was used for CV measurements in 1.0 M KOH. CV was recorded in a potential range of 1.10 V ~ 1.85 V (vs. RHE) at a scan rate of 20 mV s^{-1}. The conversion to RHE scale is by E (vs. RHE) = E (vs. Hg/HgO) + E°(Hg/HgO) + 0.059 × pH. The potential was iR corrected, in which the uncompensated resistance in the electrolyte (R) was decided by EIS (49). The reference electrode was also calibrated in H_2-saturated 1 M KOH, and the E°(Hg/HgO) was measured as 0.098 V vs. SHE.

Tafel plots are given by applied voltage (iR corrected) as a function of the current density (logarithm scale) (2) Background correction has been carried out by obtaining an average one from the polarization curves sweeping positively and negatively.

The Tafel relation is shown as following equation:

$$\eta = a + b\ \log(j), \qquad [2]$$

where η represents the overpotential (V), j is the current density (mA cm^{-2}), and b is obtained as Tafel slope.

Magneto-Electrochemical Measurement. The magneto-electrochemical measurement was performed according to our previous setup (28). Before applying magnetic field, the working electrode was cycled for 50 CVs to reach a steady CV. The working electrode chamber of the cell was then placed into the test chamber of a electromagnet instrument. Uniform magnetic field of 0.3 T was then applied to the electrolysis cell. The direction of the magnetic field in the study was fixed as out-of-plane with respect to the surface of the working electrode to mitigate the effects arising from varied magnetic field directions. CV was then carried out when the working electrode has been magnetized for 15 min, and 2 CVs were recorded under the magnetic field.

Isotope Experiment. First, Ni-shell/Fe_3O_4 was performed 50 CVs at a scan rate of 20 mV s^{-1} between 1.10 to 1.85 V vs. RHE to reach a steady CV, and a stable NiO_xH_y surface chemistry had been reached. Second, the ^{18}O-labeled shell sample was prepared by potentiostatic at 1.6 V vs. RHE for 10 min in ^{18}O-labeled 1.0 M KOH electrolyte, then rinsed by $H_2{}^{16}O$ thoroughly to remove $H_2{}^{18}O$ residue. The ^{18}O-labeled Ni-shell/Fe_3O_4 was then cycled at a scan rate of 2 mV s^{-1} in 1.0 M $K^{16}OH$ for three CVs in an air-tight cell. The gas above was collected and further analyzed by the Agilent 7890A-5977B gas chromatography-MS (GC-MS). The GC-MS experiment was run for 5 min and operated with an GC oven temperature of 110 °C and an air flow of 3 mL min^{-1}.

Data, Materials, and Software Availability. All study data are included in the article and/or *SI Appendix*.

ACKNOWLEDGMENTS. We the financial support from the A*STAR through IRG grant (M22K2c0078). Authors appreciate the Facility for Analysis, Characterisation, Testing and Simulation in Nanyang Technological University for materials characterizations.

Author affiliations: [a]School of Materials Science and Engineering, Nanyang Technological University, Singapore 639798, Singapore; [b]Department of Applied Biology and Chemical Technology, The Hong Kong Polytechnic University, Hung Hom, Kowloon, Hong Kong SAR, China; [c]Beijing National Laboratory for Molecular Engineering, College of Chemistry and Molecular Engineering, Peking University, Beijing 100871, China; [d]Institute of Sustainability for Chemicals, Energy and Environment, Agency for Science, Technology and Research, Singapore 627833, Singapore; [e]Department of Chemistry, City University of Hong Kong, Hong Kong SAR, People's Republic of China; [f]Center for Advanced Catalysis Science and Technology, Nanyang Technological University, Singapore 639798, Singapore; [g]Department of Chemical Engineering, University of Cambridge, Cambridge CB2 3RA, United Kingdom; [h]The Cambridge Centre for Advanced Research and Education in Singapore, Singapore 138602, Singapore; and [i]Energy Research Institute @Nanyang Technological University, Interdisciplinary Graduate School, Nanyang Technological University, Singapore 639798, Singapore

1. S. Yuan *et al.*, Tunable metal hydroxide–organic frameworks for catalysing oxygen evolution. *Nat. Mater.* **21**, 673–680 (2022).
2. W. Chao *et al.*, Cations in octahedral sites: A descriptor for oxygen electrocatalysis on transition-metal spinels. *Adv. Mater.* **29**, 1606800 (2017).
3. J. Suntivich, K. J. May, H. A. Gasteiger, J. B. Goodenough, Y. Shao-Horn, A perovskite oxide optimized for oxygen evolution catalysis from molecular orbital principles. *Science* **334**, 1383–1385 (2011).
4. M. T. M. Koper, Theory of multiple proton–electron transfer reactions and its implications for electrocatalysis. *Chem. Sci.* **4**, 2710–2723 (2013).
5. M. J. Craig *et al.*, Universal scaling relations for the rational design of molecular water oxidation catalysts with near-zero overpotential. *Nat. Commun.* **10**, 4993 (2019).
6. L. Gao, X. Cui, C. D. Sewell, J. Li, Z. Lin, Recent advances in activating surface reconstruction for the high-efficiency oxygen evolution reaction. *Chem. Soc. Rev.* **50**, 8428–8469 (2021).
7. L. An *et al.*, Recent development of oxygen evolution electrocatalysts in acidic environment. *Adv. Mater.* **33**, 2006328 (2021).
8. M. Yu, E. Budiyanto, H. Tüysüz, Principles of water electrolysis and recent progress in cobalt-, nickel-, and iron-based oxides for the oxygen evolution reaction. *Angew. Chem. Int. Ed.* **61**, e202103824 (2022).
9. Z.-F. Huang *et al.*, Strategies to break the scaling relation toward enhanced oxygen electrocatalysis. *Matter* **1**, 1494–1518 (2019).
10. J. Gracia, Spin dependent interactions catalyse the oxygen electrochemistry. *Phys. Chem. Chem. Phys.* **19**, 20451–20456 (2017).
11. F. A. Garcés-Pineda, M. Blasco-Ahicart, D. Nieto-Castro, N. López, J. R. Galán-Mascarós, Direct magnetic enhancement of electrocatalytic water oxidation in alkaline media. *Nat. Energy* **4**, 519–525 (2019).
12. X. Ren *et al.*, Spin-polarized oxygen evolution reaction under magnetic field. *Nat. Commun.* **12**, 2608 (2021).
13. T. Wu *et al.*, Spin pinning effect to reconstructed oxyhydroxide layer on ferromagnetic oxides for enhanced water oxidation. *Nat. Commun.* **12**, 3634 (2021).
14. T. Iida, H. Matsushima, Y. Fukunaka, Water electrolysis under a magnetic field. *J. Electrochem. Soc.* **154**, E112 (2007).
15. H. Vogt, The role of single-phase free convection in mass transfer at gas evolving electrodes–I. Theoretical. *Electrochim. Acta* **38**, 1421–1426 (1993).
16. J. Gracia, Itinerant spins and bond lengths in oxide electrocatalysts for oxygen evolution and reduction reactions. *J. Phys. Chem. C* **123**, 9967–9972 (2019).
17. J. Gracia, R. Sharpe, J. Munarriz, Principles determining the activity of magnetic oxides for electron transfer reactions. *J. Catal.* **361**, 331–338 (2018).
18. X. Li, Z. Cheng, X. Wang, Understanding the mechanism of the oxygen evolution reaction with consideration of spin. *Electrochem. Energy Rev.* **4**, 136–145 (2021).
19. X. Ren *et al.*, The origin of magnetization-caused increment in water oxidation. *Nat. Commun.* **14**, 2482 (2023).
20. H. Khurshid *et al.*, Synthesis and magnetic properties of core/shell FeO/Fe_3O_4 nano-octopods. *J. Appl. Phys.* **113**, 17B508 (2013).
21. J. Ge *et al.*, Ferromagnetic-antiferromagnetic coupling core-shell nanoparticles with spin conservation for water oxidation. *Adv. Mater.* **33**, 2101091 (2021).
22. Y. Chen *et al.*, Exceptionally active iridium evolved from a pseudo-cubic perovskite for oxygen evolution in acid. *Nat. Commun.* **10**, 572 (2019).
23. G. Zhao, P. Li, N. Cheng, S. X. Dou, W. Sun, An Ir/$Ni(OH)_2$ heterostructured electrocatalyst for the oxygen evolution reaction: Breaking the scaling relation, stabilizing iridium (V), and beyond. *Adv. Mater.* **32**, 2000872 (2020).
24. X. Ren *et al.*, Constructing an adaptive heterojunction as a highly active catalyst for the oxygen evolution reaction. *Adv. Matter* **32**, e2001292 (2020).
25. J. Ge *et al.*, Ferromagnetic-antiferromagnetic coupling core-shell nanoparticles with spin conservation for water oxidation. *Adv. Matter* **33**, e2101091 (2021).
26. N. Weidler *et al.*, X-ray photoelectron spectroscopic investigation of plasma-enhanced chemical vapor deposited NiO_x, $NiO_x(OH)_y$, and $CoNiO_x(OH)_y$: Influence of the chemical composition on the catalytic activity for the oxygen evolution reaction. *J. Phys. Chem. C* **121**, 6455–6463 (2017).
27. S. Klaus, Y. Cai, M. W. Louie, L. Trotochaud, A. T. Bell, Effects of Fe electrolyte impurities on $Ni(OH)_2$/NiOOH structure and oxygen evolution activity. *J. Phys. Chem. C* **119**, 7243–7254 (2015).
28. C. Wei, Z. J. Xu, The possible implications of magnetic field effect on understanding the reactant of water splitting. *Chin. J. Cataly.* **43**, 148–157 (2022).
29. Q. Li *et al.*, Correlation between particle size/domain structure and magnetic properties of highly crystalline Fe_3O_4 nanoparticles. *Sci. Rep.* **7**, 9894 (2017).
30. A. Berkowitz, K. Takano, Exchange anisotropy–A review. *J. Magnet. Magnet. Mater.* **200**, 552–570 (1999).
31. J. Nogués, I. K. Schuller, Exchange bias. *J. Magnet. Magnet. Mater.* **192**, 203–232 (1999).
32. H. N. Nong *et al.*, Key role of chemistry versus bias in electrocatalytic oxygen evolution. *Nature* **587**, 408–413 (2020).
33. T. Wu, Z. J. Xu, Oxygen evolution in spin-sensitive pathways. *Curr. Opin. Electrochem.* **30**, 100804 (2021).
34. M. J. Craig *et al.*, Universal scaling relations for the rational design of molecular water oxidation catalysts with near-zero overpotential. *Nat. Commun.* **10**, 1–9 (2019).
35. X. Li, P. E. Siegbahn, Water oxidation mechanism for synthetic Co–Oxides with small nuclearity. *J. Am. Chem. Soc.* **135**, 13804–13813 (2013).
36. M. T. Swann, K. M. Nicholas, Structural effects on dioxygen evolution from Ru (V)–Oxo complexes. *Eur. J. Inorgan. Chem.* **2021**, 3565–3577 (2021).
37. Z. Devizorova, S. Mironov, A. Buzdin, Theory of magnetic domain phases in ferromagnetic superconductors. *Phys. Rev. Lett.* **122**, 117002 (2019).

38. C. Kittel, Physical theory of ferromagnetic domains. *Rev. Mod. Phys.* **21**, 541–583 (1949).
39. M. Müllner *et al.*, Stability and catalytic performance of reconstructed Fe_3O_4(001) and Fe_3O_4(110) surfaces during oxygen evolution reaction. *J. Phys. Chem. C* **123**, 8304–8311 (2019).
40. A. Grimaud *et al.*, Activating lattice oxygen redox reactions in metal oxides to catalyse oxygen evolution. *Nat. Chem.* **9**, 457–465 (2017).
41. T. Wu *et al.*, Iron-facilitated dynamic active-site generation on spinel $CoAl_2O_4$ with self-termination of surface reconstruction for water oxidation. *Nat. Cataly.* **2**, 763–772 (2019).
42. L. Wang *et al.*, Catalysis and in situ studies of $Rh1/Co_3O_4$ nanorods in reduction of NO with H_2. *Acs Cataly.* **3**, 1011–1019 (2013).
43. Y. Du *et al.*, XAFCA: A new XAFS beamline for catalysis research. *J. Synchrotron Radiat.* **22**, 839–843 (2015).
44. B. Ravel, M. Newville, Athena, artemis, hephaestus: Data analysis for X-ray absorption spectroscopy using IFEFFIT. *J. Synchrotron Radiat.* **12**, 537–541 (2005).
45. G. Kresse, J. Furthmüller, Efficient iterative schemes for ab initio total-energy calculations using a plane-wave basis set. *Phys. Rev. B.* **54**, 11169 (1996).
46. J. P. Perdew, K. Burke, M. Ernzerhof, Generalized gradient approximation made simple. *Phys. Rev. Lett.* **77**, 3865 (1996).
47. S. L. Dudarev, G. A. Botton, S. Y. Savrasov, C. Humphreys, A. P. Sutton, Electron-energy-loss spectra and the structural stability of nickel oxide: An LSDA+ U study *Phys. Rev. B* **57**, 1505 (1998).
48. H. J. Monkhorst, J. D. Pack, Special points for Brillouin-zone integrations. *Phys. Rev. B* **13**, 5188 (1976).
49. C. Wei *et al.*, Recommended practices and benchmark activity for hydrogen and oxygen electrocatalysis in water splitting and fuel cells. *Adv. Mater.* **31**, 1806296 (2019).